

Role of Catalyst on Refractive Index Tunability of Porous Silica Antireflective Coatings by Sol–Gel Technique

Abhilash Vincent, Suresh Babu, Erik Brinley, Ajay Karakoti, Sameer Deshpande, and Sudipta Seal*

Advanced Material Processing and Analysis Center (AMPAC), Mechanical, Materials, and Aerospace Engineering, University of Central Florida, 4000 Central Florida Boulevard, Orlando, Florida 32816

Received: January 4, 2007; In Final Form: April 19, 2007

Porous silica coatings were prepared by acid- and base-catalyzed sol–gel method. Surface morphology studies by atomic force microscopy showed smooth surface for acid-catalyzed coatings while base catalysis resulted in coarse particle morphology. On increasing the tetraethyl orthosilicate to base molar ratio from 1:1 to 1:3, the mean particle size of the coating shifted from 30 to 100 nm while the pore size varied from 4.7 to 14 nm. Infrared spectral analysis exhibited a change in the ratio of integrated peak intensities of Si–O–Si to Si–OH in acid- and base-catalyzed silica coatings. Textural studies showed an increase in particle size and porosity with base concentration. Optical transmission and surface roughness of base-catalyzed samples were found to be higher than that of acid-catalyzed silica coatings.

Introduction

Antireflective (AR) coatings play an important role in a variety of optical technologies by reducing the reflective losses at the interfaces. AR coatings have been widely used in many energy-related applications such as solar thermal and photovoltaic systems. In the case of devices, such as flat panel display, AR coatings are used to reduce transmission losses.¹ There are several approaches to introduce antireflectance, and among them, the coating with an adjustable refractive index on the substrate is a prominent one. An ideal homogeneous antireflective coating can achieve effectively 0% reflection at a specific wavelength when its refractive index (n_c) is equal to $(n_1 n_2)^{1/2}$, where n_1 and n_2 are the refractive indices of the air and the substrate, respectively.² A typical glass has an index of refraction between 1.45 and 1.65 in visible spectral region, which implies that the index of refraction of the antireflective interference film must be between 1.20 and 1.25.³ Such a low-index requirement makes it practically impossible to design a dense single-layer AR film on glass. Further, the low refractive index is difficult to attain with any known low-index coating material (the lowest index optical material is MgF₂ with $n = 1.38$ at 600 nm).⁴ Since the refractive index of a material is related to its density, the index can be lowered by introducing porosity, provided that the pore sizes are much smaller than the electromagnetic wavelengths of interest. The refractive index is related to the porosity according to the Lorentz–Lorenz relationship⁵

$$\frac{(n_f^2 - 1)}{(n_f^2 + 2)} = (1 - V_f) \frac{(n_s^2 - 1)}{(n_s^2 + 2)} \quad (1)$$

where n_f and n_s are the refractive indices of the porous film and the solid skeleton, respectively, and V_f is the volume fraction of the pores. Thus, by tuning the porosity, hence refractive index of the coating, it is possible to tune the antireflective properties of any substrate material.

The materials widely used as AR coatings are dielectric materials such as silica, titania, and alumina with refractive indices of 1.45, 2.3, and 1.65, respectively, in the midvisible range spectral region. Silica coating has low refractive index, good durability, and environmental resistance.⁶ As a result of tunable refractive index properties, porous silica is considered to be one of the best antireflective coatings^{7,8} which attracted wider interest in optical, microelectronic, and thermal applications.^{9–13} To introduce porosity in thin films, broadly three approaches can be followed: (1) by introducing organic filler particles as templates that can be removed later to create the porosity, (2) by coating made up of larger particles, and (3) by the use of bimodal size distribution.¹⁴ Sol–gel technique is one of the widely used techniques for the formation of porous coatings. Sol–gel technique gives a greater control on pore size as pore size can be modified by tuning the process parameters.^{6,15,16} While the use of filler particles for introducing porosity led to poor mechanical properties,^{17,18} porous silica coatings developed through colloidal sol–gel route were reported to be stress-free and highly damage resistant.^{18,19} Acid or base or a combination of acid and base has been used as catalyst to form the porous silica coatings.^{16–18} However, still a comprehensive understanding relating the role of catalyst and catalyst concentration with surface and optical properties is limited.

In the present study, we have used acid and base catalysis for the fabrication of antireflective porous silica coatings with a transmission of about 99% on boron silicate glass. The effect of catalyst nature and concentration on porosity, surface roughness, and microstructural and optical transmittance has been reported.

Experimental Section

Materials. Porous silica coatings were prepared by sol–gel method using tetraethyl orthosilicate (TEOS, Sigma Aldrich, 98%) as precursor and ethanol as the solvent (Sigma Aldrich, 99.5%). The molar ratio of TEOS to ethanol was maintained at 1:30 for all the experiments and either a base (ammonia) or an

* To whom correspondence should be addressed. E-mail: sseal@mail.ucf.edu.

TABLE 1: Details of Synthesis Parameters for the Preparation of Porous Silica

coating	molar ratio of TEOS to catalyst	viscosity (mPa s)	aging time (h)
BC11	1:1	1.92	72
BC12	1:2	1.87	30
BC13	1:3	1.84	18
AC	1:0.025	2.56	18

acid (nitric acid) was used as a catalyst. Depending on the nature of catalyst (acid or base), the samples were coded as AC or BC. All solutions were aged for different time periods to ensure completion of condensation reaction depending on the concentration of the catalyst to form a sol optimum for coating. Table 1 summarizes the sample codes and the corresponding variation in molar ratio, viscosity, and aging time for both acid- and base-catalyzed samples. Viscosity measurements were carried out using HAAKE Viscotester 7 rotational viscometer, at 25 °C and at a shear rate of 244.8 s⁻¹. The coatings were made on glass slides by dip-coating technique (Dip Coater, 1000 IUD, KSV Instruments Ltd., Finland) at a withdrawal rate of 8.5 cm/min. Boron silicate glass (BK-7) having a refractive index close to 1.53 at 550 nm was used as substrate. The glass slides used as substrate for coating were ultrasonicated in acetone for 10 min. The coatings were dried at room temperature in air under normal atmospheric conditions for 12 h.

Surface and Optical Characterization. The surface topography and the microstructure of the coatings were studied with a Multimode AFM (MMAFM-2, Nanoscope IIIa Digital Instruments) in tapping mode using a 7 nm radius silicon tip (PPP-NCH, Nanosensors). The surface root-mean-square (rms) roughness values were obtained from the analysis of atomic force microscopy (AFM) images. Solver PRO Scanning Probe Microscope (NT-MDT) was used to perform the coating scratch-resistant measurements. The coating thickness and refractive index was calculated from the optical transmission spectra by simulation using Film Star (FTG Software Associates) software. Ellipsometry measurements were used (VASE Spectroscopic Ellipsometer) to validate the calculated thickness and refractive index from the simulation. Transmittance of silica coatings was measured with a UV-vis spectrophotometer (Varian, CARY 1E) over a spectral range of 200–900 nm. Attenuated total reflectance–Fourier transformed infrared (ATR-FTIR) spectroscopy was used for evaluating structural modifications. ATR-FTIR spectra were recorded in a Perkin-Elmer (Spectrum one) FTIR spectrometer in the range of 4000–600 cm⁻¹. Surface area measurements were carried out to obtain the texture properties (surface area and pore volume) using a NOVA 4200e surface area and pore size analyzer. The silica samples were degassed at 378 K for 12 h, and the adsorption–desorption isotherms were obtained at 77 K. The surface area was calculated using Brunauer–Emmett–Teller (BET) method, and the average pore radius (*r*) and pore size distributions (PSD) were calculated by the Barrett–Joyner–Halenda (BJH) method.

Results and Discussion

Surface Morphology of the Films. AFM patterns of the surface morphologies of silica films for AC, BC11, BC12, and BC13 are shown in Figure 1. AFM images exhibited a direct relation between the surface morphology with the nature and concentration of catalyst. The acid-catalyzed coating (AC) exhibited smooth and dense surface while base-catalyzed coatings showed rough and coarse particle morphology. Among the three base-catalyzed samples, BC11 showed finer particles while BC13 showed coarser particles. With the increase in base

concentration, there was a corresponding increase in particle size. Even a lower molar ratio of acid catalyst (AC in Table 1) resulted in smooth surface morphology, and further increase in acid catalyst concentration did not result in marked variation of surface morphology. Apart from the one acid-catalyzed silica sample mentioned as coating AC in Table 1, two different concentrations, one with lower and one with higher acid content, were prepared with molar ratios of 1:0.0125 and 1:0.0375. Optical transmission and particle size of these coatings remained the same and were found to be independent of the amount of acid catalyst. However, a trend of transition from an ultrasmooth to a slightly clustered network structure was observed with increase in acid content. Since changes in acid content have marginal influence on the morphology and transmission, only coating AC is reported here. Particle size distributions calculated from the AFM images (Figure 1) are shown in Figure 2. The mean particle size was found to be 5, 30, 55, and 100 nm for AC, BC11, BC12, and BC13, respectively. The surface studies showed a direct relation of particle morphology on the acidic/basic nature of catalyst in the precursor solution.

Surface Chemical Analysis. To understand the chemical modifications occurring over the surface of the silica thin films, infrared spectral analysis was carried out. ATR-FTIR spectra of porous silica formed from base- and acid-catalyzed silica sol-gel in the regime of 600–1400 cm⁻¹ are shown in Figure 3. The Si–O–Si vibrational modes, ascribed to symmetric stretching (TO₂) and asymmetric stretching (TO₃), were observed at about 800 cm⁻¹ and 1060 cm⁻¹, respectively. A strong shoulder observed at about 1150 cm⁻¹ is related to the longitudinal optical component (LO₃) of the high-frequency vibration of SiO₂. All the samples exhibited a band near 940 cm⁻¹, which is assigned to stretching vibrations of Si–OH bonds. The absence of peak at 1400 cm⁻¹ indicates that no residual ethoxy groups were present. Figure 4 shows the ATR-FTIR spectra of porous silica samples in the regime of 4000–1500 cm⁻¹. An O–H stretching region is observed near 3400 cm⁻¹ (Figure 4) where both H₂O (3300 cm⁻¹) and SiOH (3650 cm⁻¹) components are apparent.²⁰ An O–H bending vibration of water molecule is observed at 1630 cm⁻¹²¹ (Figure 4). Intensity of Si–O–Si and Si–OH peaks increases with increase in concentration of base catalyst. AC and BC11 showed low intense Si–O–Si and Si–OH peaks in comparison to BC12 and BC13.

To delineate the intensities of Si–O–Si and Si–OH with the influence of catalyst, a Gaussian curve fit was carried out for all the coatings. Figure 5 shows a Gaussian curve fit for the base-catalyzed sample BC13. After resolving individual peaks, the area under the peak was calculated toward their integrated intensity. Ratio of integrated intensity of Si–O–Si to Si–OH peaks at positions 1060 cm⁻¹ and 940 cm⁻¹, respectively, was calculated. Calculated Si–O–Si to Si–OH ratio was found to be 1.85, 2, 2.4, and 2.6 for AC, BS11, BS12, and BS13 samples, respectively. Acid-catalyzed silica coating (AC) showed the lowest ratio while the ratio shifted from 2 to 2.6 with the concentration of base catalyst. The relative increase in the peak-integrated intensity ratio shows an increase in formation of Si–O–Si and a corresponding decrease in Si–OH intensity. In other words, an increase in base catalyst concentration increases the rate of condensation reaction of silanol group (Si–OH) to form siloxane groups (Si–O–Si).

Synthesis of silica by sol-gel process involves the formation of a colloidal suspension of siloxane groups (Si–O–Si) by condensation reaction of water with silanol (Si–OH). The mechanistic aspects of hydrolysis, alcohol, and water condensation reactions are widely available in literature.^{22,23} The polym-

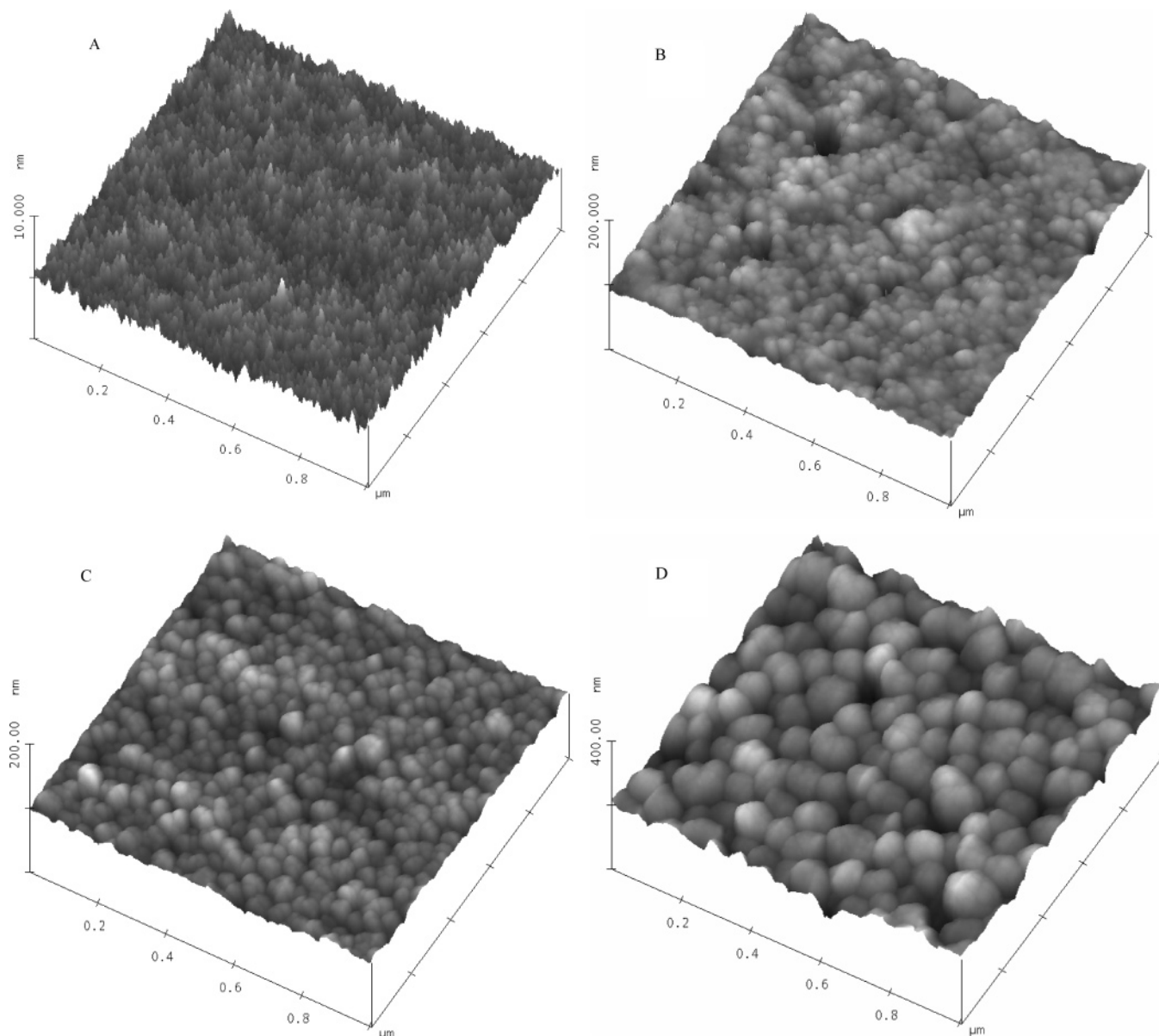


Figure 1. AFM images of acid- and base-catalyzed silica coatings on BK-7 glass substrate: (A) AC, (B) BC11, (C) BC12, and (D) BC13. Particle size increases with increase in the basic nature of the catalyst. All the images are taken at $1 \mu\text{m} \times 1 \mu\text{m}$ area at a scan rate of 1 Hz.

erization stages can be described as (1) polymerization of monomers to form primary particles, (2) growth or agglomeration of primary particles into larger particles, and (3) linking of particles into chains to form a three-dimensional network that extends throughout the liquid medium leading into a gel formation.^{22,23} The presence of acid or base catalyst has profound effect on the mechanism of the reaction and the final morphology.

Under acidic conditions, the alkoxide group is protonated in the first step. Si in the alkoxide becomes more electrophilic and starts reacting with the surrounding water molecule. The water molecule attacks from the rear and acquires a partial positive charge. At the same time, the positive charge of the protonated alkoxide is correspondingly reduced resulting in the formation of a pentacoordinate transition state with significant $\text{S}_{\text{N}}2$ (substitution nucleophilic bimolecular) type character. At the end of the reaction, alcohol leaves as a byproduct followed by inversion of silicon tetrahedron²² (Scheme 1). This hydrolysis reaction is followed by polymerization reaction to form siloxane bonds by either an alcohol-producing or water-producing condensation reaction. The sequence of condensation requires

both depolymerization (ring opening) and addition of monomers.²² The rate of ring-opening polymerizations and monomer addition reaction is dependent upon the solution pH. In this acidic pH range ($\text{pH} < 7$), the solubility of silica is very low and the particle growth stops when the particle reaches about 5 nm where the solubility and the size-dependence solubility are greatly reduced. Thus, the resulting linear chain network will be composed mostly of small primary particles. This is in agreement with our AFM results (Figure 1A). In the base-catalyzed condition, the water dissociates to produce nucleophilic hydroxyl anions in a rapid first step. Here, also, an $\text{S}_{\text{N}}2$ reaction mechanism is composed of the hydroxyl anion attacking the silicon atom and displacing the OR^- with inversion of the silicon tetrahedron²² (Scheme 2).

The growth occurs primarily through the addition of monomers to the more highly condensed particles rather than by particle aggregation. Because of greater solubility of silica and greater size dependence of silica above $\text{pH} = 7$, these larger particles grow by Ostwald ripening²³ mechanism whereby the particles grow in size and decrease in number as highly soluble small particles dissolve and precipitate again into larger less

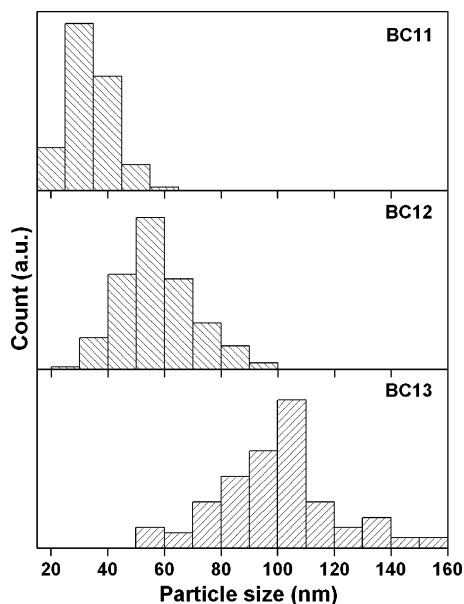


Figure 2. Particle size distribution of base-catalyzed silica samples BC11, BC12, and BC13 obtained from AFM images shown in Figure 1. Particle size increases with increase in base catalyst concentration.

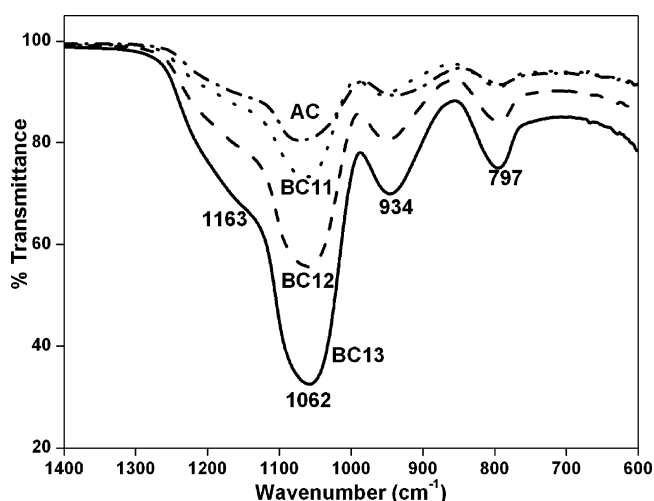


Figure 3. ATR-FTIR spectra of acid- and base-catalyzed silica samples in the regime of 1400–600 cm^{-1} .

soluble particles. The growth stops when the difference in the solubility between the smallest and the largest particle becomes negligible. This type of growth results in highly branched silica cluster formation, as the particles are negatively charged and repel each other to form particulate sol. This is in agreement with our AFM images of base-catalyzed coatings (Figure 1B, 1C, and 1D). Thus, acid catalysis resulted in dense film because of the formation of polymeric chains while base catalysis led to porous film through particulate network formation. This is in agreement with the surface morphologies obtained from AFM studies.

Textural Properties. The textural properties (surface area, pore volume, pore size distribution) measurements were carried out on acid- and base-catalyzed silica samples. The pore size distributions (PSD) of acid- and base-catalyzed silica powders are shown in Figure 6. The sample AC (acid-catalyzed) shows a smooth surface while base-catalyzed samples showed a wider distribution. Further, the mean pore size shifted to larger values for base-catalyzed samples. The observation of catalyst assisted tuning of PSD is in good agreement with the recent report.²⁴

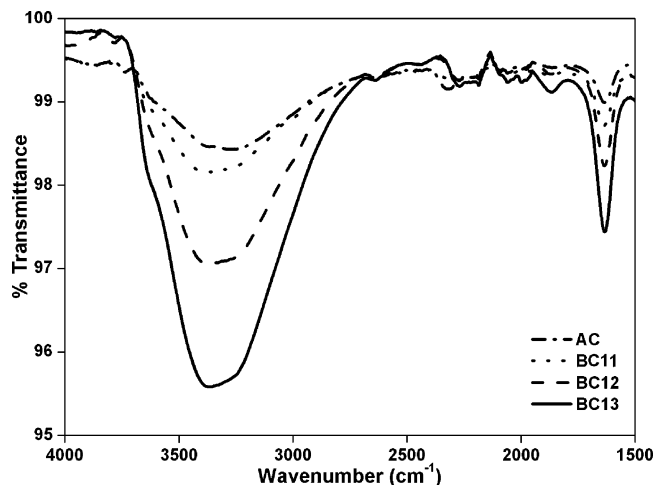


Figure 4. ATR-FTIR spectra of acid- and base-catalyzed samples in the regime of 4000–1500 cm^{-1} .

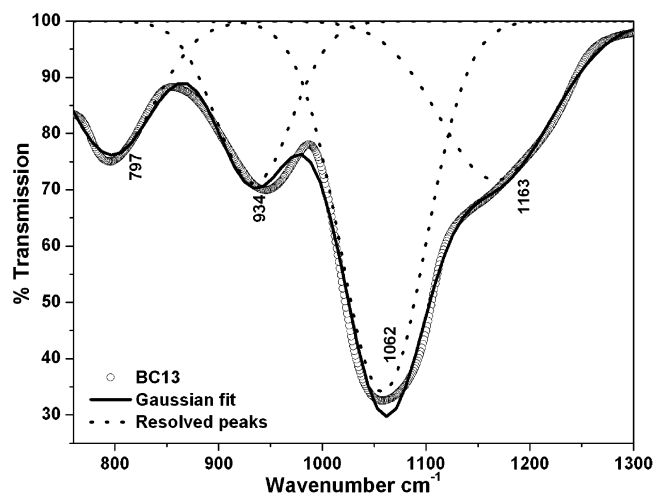


Figure 5. Gaussian peak fitting of the ATR-FTIR spectra for coating BC13; individual peaks are resolved for relative intensity calculation.

The textural properties of acid- and base-catalyzed silica samples are summarized in Table 2. BC11 powder showed higher surface area ($\sim 595 \text{ m}^2/\text{g}$) and highest porosity (49%) among all powders. This is due to the small particle size nature ($\sim 34 \text{ nm}$) of BC11. However, BC13 powder composed of larger silica particles ($\sim 100 \text{ nm}$) showed the lowest surface area ($\sim 264 \text{ m}^2/\text{g}$) and porosity (36%) among the base-catalyzed samples, and the pore size of BC13 was more comparable to that of BC11 and BC12. Figure 7 shows the AFM image of BC13 silica with pore centers trapped between silica particles (indicated by arrows). BC12 powder ($\sim 57 \text{ nm}$ size particles) has a surface area in-between BC11 and BC13 ($\sim 357 \text{ m}^2/\text{g}$) with a porosity of 42%. AC powders showed the lowest surface area ($\sim 199 \text{ m}^2/\text{g}$) and lowest porosity (5%) among all the powders. Acid-catalyzed silica coatings result in atomically smooth coatings (rms roughness $\sim 0.34 \text{ nm}$). These coatings form a strongly bonded network structure which gives them high mechanical strength. Their low surface area in powder form can be correlated to their lower surface roughness in the case of thin film form. The density of porous silica is calculated from the pore volume fraction and bulk density of silica powder.

The density of porous silica obtained from base-catalyzed silica increased as the concentration of base catalyst was increased. This is due to the formation of larger silica particles. As the particle starts growing, they form more and more dense particles which are devoid of any pores. This is the reason for

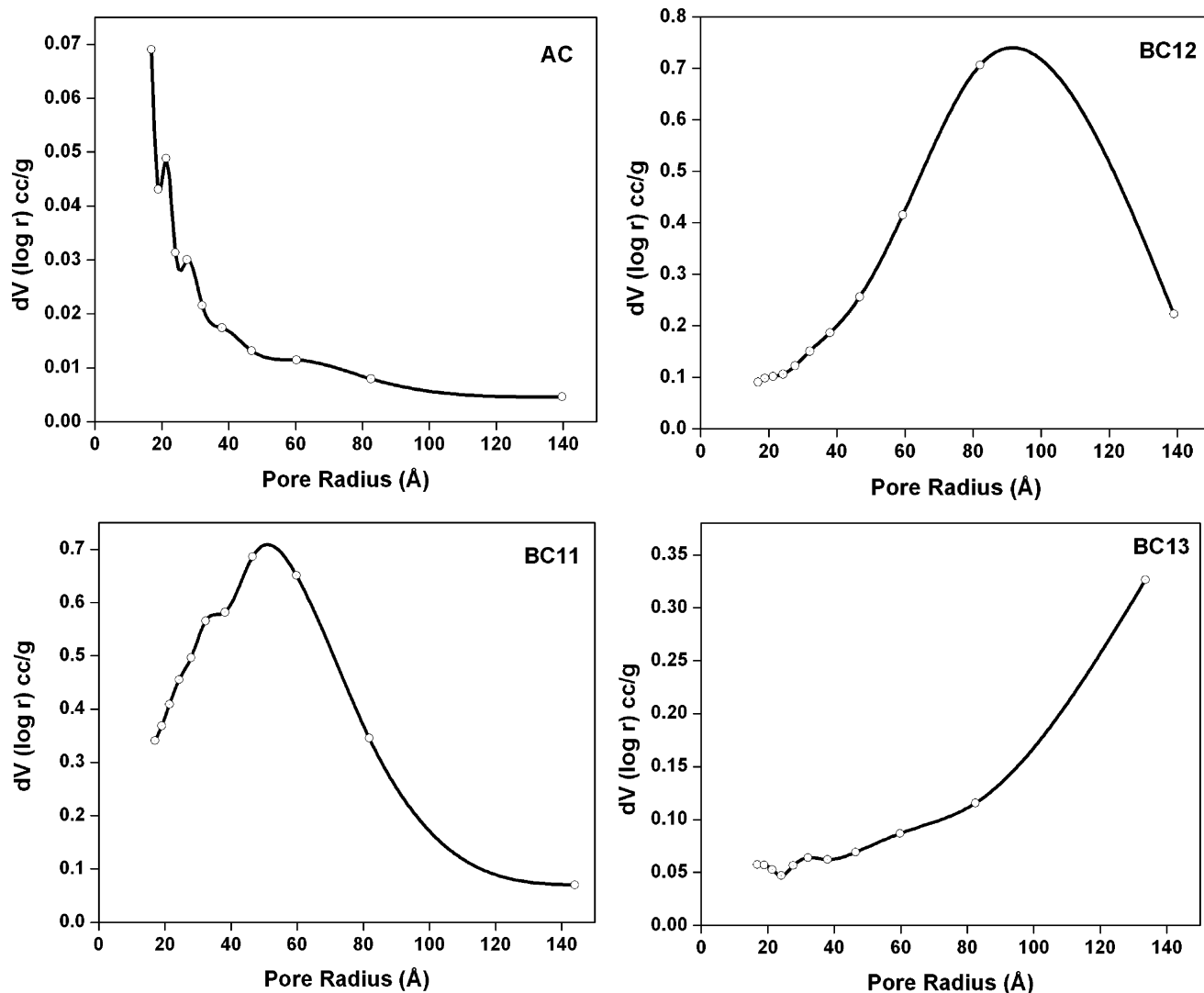
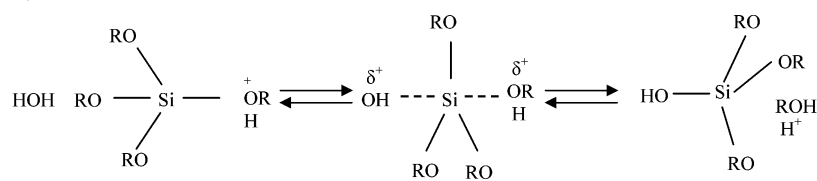
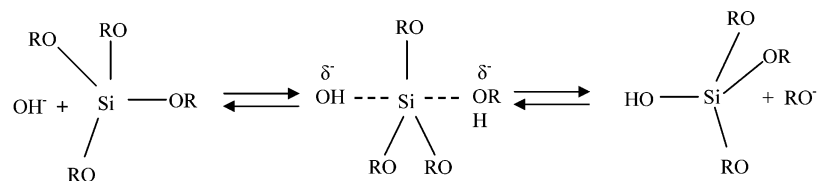


Figure 6. Pore size distribution (PSD) profiles of the acid- and base-catalyzed silica samples.

SCHEME 1: Acid-Catalyzed Reaction Mechanism of Sol–Gel Silica



SCHEME 2: Base-Catalyzed Reaction Mechanism of Sol–Gel Silica



increase in density of porous silica with base catalyst concentration. Acid-catalyzed silica showed the highest density (2.18 g/cm^3) among all the samples. This is due to the formation of highly dense network structure which had much lower porosity (5%) and is close to the bulk density (2.3 g/cm^3) of silica.

AFM scratch-resistant measurements were conducted on these coatings to determine the resistance to low-load scratching. W₂C coated AFM tip of 30 nm curvature radius (NSG 20/W2C, NT-MDT) was used to scratch the coatings. Base-catalyzed silica

coatings showed no resistance to scratch and exhibited a scratch depth closer to their film thickness ($\sim 100 \text{ nm}$) at a load of $10 \mu\text{N}$, while acid silica coatings were highly resistant to scratch and exhibited a scratch depth of $\sim 2 \text{ nm}$ even at a load of $40 \mu\text{N}$. Acid-catalyzed coatings were composed of smaller (less than 2 nm) particles with many more particle–particle bondings resulting in higher coating strength. Base-catalyzed silica coatings composed of larger particles with weaker and lower number of particle–particle bonding exhibited decreased coating strength.²⁵

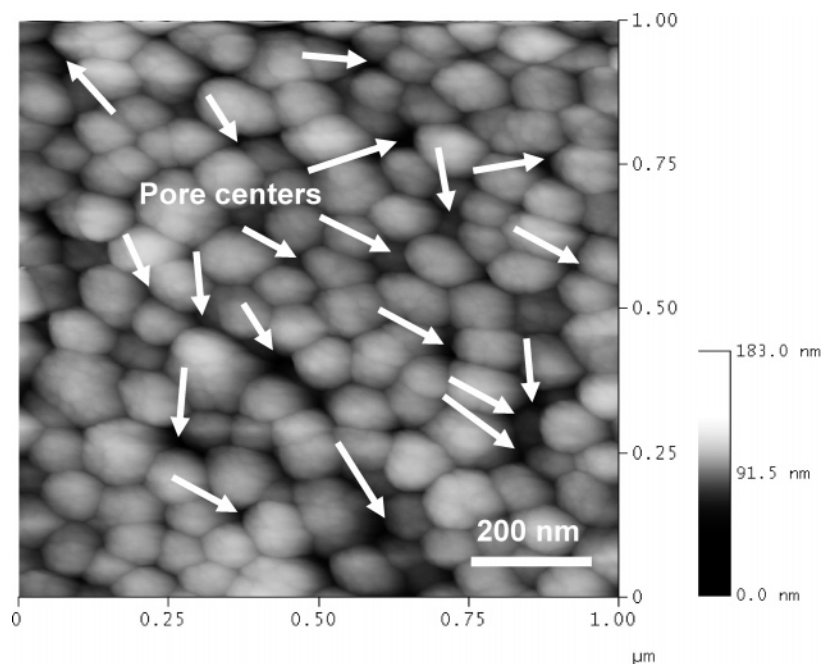


Figure 7. AFM image of base-catalyzed silica (BC13) coating with pores in-between silica particles. Arrows indicate the pore centers.

TABLE 2: Textural Properties of Acid- and Base-Catalyzed Silica Powder

coating	surface area (m ² /g)	pore volume (cc/g)	pore radius (nm)	porosity (%)	density (g/cc) of porous silica
AC	198.87	0.02	1.7	5.0	2.18
BC11	594.46	0.42	4.7	49.1	1.17
BC12	356.61	0.32	8.2	42.2	1.33
BC13	263.97	0.25	14	36.1	1.47

Surface Roughness of the Films. The surface topographies of both the substrate and the film determine the quality of the coating in terms of their optical transmission.²⁶ The surface morphology of the coatings can lead to surface scattering and can reduce the transmitted intensity. Optical transmission through a rough surface is considerably affected by scattering of light having wavelengths close to the magnitude of the surface features. The optical scattering loss at a rough interface between two media is described by the scalar scattering theory.^{27–29} The corresponding scattering loss in transmitted intensity is given by

$$T^s = T_0 \left\{ 1 - \exp \left[- \left(\frac{2\pi(n_1 - n_2)R_q}{\lambda} \right)^2 \right] \right\} \quad (2)$$

and the surface scattering coefficient is given by

$$\alpha_{\text{surf}}(\lambda) = \left[\frac{2\pi(n_1 - n_2)R_q}{\lambda} \right]^2 \quad (3)$$

where T_0 , λ , R_q , n_1 , and n_2 are the total transmittance, optical wavelength, rms surface roughness, and refractive index of film and air, respectively.²⁶ To quantify the surface topography, roughness measurements on the coatings were made using AFM. Table 3 shows the roughness and the particle size of these coatings. The root-mean-square (rms) surface roughness of the base-catalyzed silica increases with increase in base concentration because of an increase in the particle size (Table 3). As the particle size increases, the surface packing density decreases, void space increases between the particles, and the surface becomes rougher. Among the base-catalyzed silica films, BC13 had the highest roughness about 16 nm. In the case of acid-

TABLE 3: Surface Roughness and Particle Size of Optical Coatings from AFM Image Analysis

coating	rms roughness (nm)	particle diameter (nm)	$\alpha_{\text{surf}}(\lambda)$ at 550 nm	% T_s/T_0
AC	0.3	5.9 ± 1.1	3.0×10^{-6}	3.0×10^{-4}
BC11	4.5	33.5 ± 8.8	5.2×10^{-4}	5.2×10^{-2}
BC12	10.6	57.1 ± 12.9	2.9×10^{-3}	2.9×10^{-1}
BC13	16.2	99.5 ± 20.7	6.7×10^{-3}	6.7×10^{-1}

catalyzed silica, the surface roughness is less (0.3 nm). This is because, when the particle size becomes smaller, the packing density increases and the surface becomes smooth (Table 2, Figure 1A). With the increase in particle size and film surface roughness, optical scattering loss also increases. It is clear from Table 3 that the scattering loss of AS is much less while BC13 showed the highest scattering loss among all samples. The scattering loss due to surface roughness in the transmitted intensity is less than 1% for all the samples, which is too low to affect any transmission loss. Since rms surface roughness of all these films is less than 20 nm, this roughness is small enough not to cause any intense surface light scattering as long as the wavelength is longer than 200 nm.³⁰

Optical Properties of the Sol–Gel Coatings. UV–vis optical transmission spectra of the acid- and base-catalyzed sol–gel silica coatings are shown in Figure 8. Base-catalyzed silica coatings showed high optical transmission in the visible wavelength range, while acid-catalyzed silica coatings exhibited lower optical transmission. The base-catalyzed sol–gel silica with a TEOS to NH₄OH ratio of 1:1 (BC11) resulted in a transmission of 99.03% at 548 nm compared to that of the acid-catalyzed silica (a transmission of 95.50%). This enhanced transmission is due to the lower refractive index of the base-catalyzed silica, compared to the former, which is necessary to produce higher transmission on boron silicate glass. This observation can be correlated with the structural morphology the coatings (Figure 1). As discussed earlier, the base-catalyzed hydrolysis resulted in larger silica particles, and the silica coatings prepared from the sol–gel solution have larger pores and higher surface roughness. The porous centers can trap air and can result in an inhomogeneous refractive index coating. Since the refractive index of air is considered as unity,

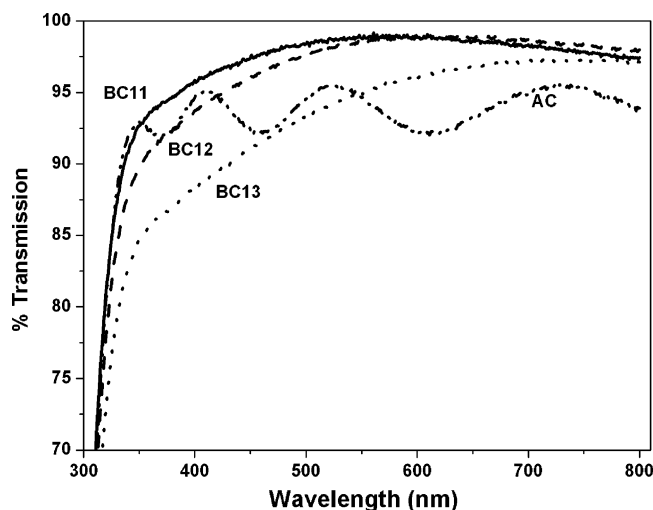


Figure 8. Transmission spectra of acid- and base-catalyzed sol-gel silica coatings on glass substrate. BC11 showed the highest transmission among all the samples (99.03% at 548 nm).

incorporation of air in highly porous coatings can result in a lower refractive index compared to that of less porous coatings. Although it is expected that BC13 sample should show higher transmission compared to other samples, it exhibited a lower value. In BC13, the coating is composed of 100 nm diameter silica clusters, and the sizes of the void space between these clusters are comparable to the size of the clusters. With the increase in void space, there will be a corresponding increase in light scattering at wavelengths closer to their size. This results in lower transmission of BC13 compared to that of BC11.³

Evaluation of Refractive Index and Thickness of the Coatings. The refractive index of these coatings can be calculated by constructing continuous envelopes T_M and T_m around the maxima and the minima of the interference fringes.³¹ If the substrate refractive index is s , the value of film refractive index, n , is given by³²

$$n^2 = N + (N^2 - s^2)^{1/2} \quad (4)$$

where

$$N = 2s \frac{T_M - T_m}{T_M T_m} + \frac{s^2 + 1}{2} \quad (5)$$

If n_1 and n_2 are the refractive indices at two adjacent maxima (or minima) at λ_1 and λ_2 , the thickness d is given by

$$d = \frac{\lambda_1 \lambda_2}{2(\lambda_1 n_2 - \lambda_2 n_1)} \quad (6)$$

Film Star (FTG Software Associates) software was used to model the refractive index and the thickness of these coatings and matched well with the experimental results obtained from ellipsometric measurements. Figure 9 shows a comparison of the experimental data versus theoretical transmission spectra

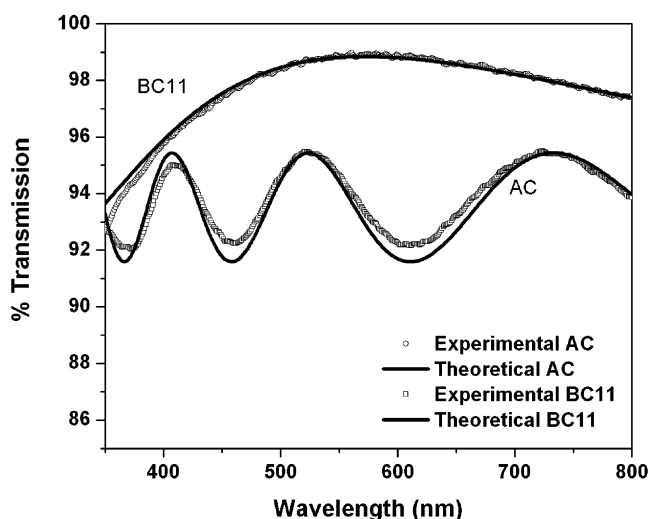


Figure 9. Comparison of theoretical and experimental transmission spectra of base- and acid-catalyzed silica coatings on glass substrate.

of the base- and acid-catalyzed sol-gel silica coatings. The theoretical profile agrees well with the experimental results.

The acid-catalyzed sol-gel silica coatings are usually denser in nature compared to that of the base-catalyzed silica coatings. The multiple interference peaks of the acid-catalyzed silica coating showed that these coatings were thicker in nature, while the base-catalyzed silica coatings were thin as indicated by their transmission spectra. Film thickness increases with viscosity and dip-coating speed (pull or drain rate).³³ Both acid and base silica coatings were prepared with the same withdrawal rate of 8.5 cm/min. The variation in thickness between acid- and base-catalyzed silica can be directly correlated to the viscosity of the sol-gel solution (Table 1). Viscosity of acid-catalyzed silica was 2.66 mPa s while that of base-catalyzed silica varied between a close range of 1.92–1.84 mPa s. In the case of acid-catalyzed silica, a strongly bonded network structure makes the sol more viscous than the loosely bonded particulate structure obtained in the case of base-catalyzed silica.²⁵ Among the base-catalyzed silica, BC11 showed higher viscosity while BC13 showed lower viscosity. This can be correlated to the presence of higher interaction forces between larger concentration of small silica particles as compared to that of BC12 and BC13 where the interaction forces are low because of smaller concentration of large-size silica particles.³⁴ However, the variation in viscosity among the base-catalyzed silica sol-gel solutions was marginal and insufficient to produce a noticeable thickness variation among base-catalyzed silica-coated samples. Table 4 presents the calculated thickness, refractive index, and other optical properties of the films. The calculations also showed that the refractive index of the sol-gel silica coatings were less than that of the substrate, which is a different form of silica and is highly dense in nature. The lower refractive index of sol-gel silica is due to the effect of the incorporation of porosity. Acid-catalyzed silica coatings showed a higher refractive index (1.443 at 550 nm) compared to that of base-catalyzed silica coatings (1.335 at 550 nm) over the substrates of boron silicate microscopic glass slides (1.53 at 550 nm). The maximum

TABLE 4: Optical Properties of Silica Coatings Made by Acid- and Base-Catalyzed Sol-Gel Chemistry

coating	thickness	refractive index	maximum % transmission	wavelength of maximum transmission
AC	635 ± 2 nm	1.443 ± 0.001	95.5	521 nm
BC11	110 ± 2 nm	1.335 ± 0.001	99.0	548 nm
BC12	107 ± 2 nm	1.340 ± 0.001	99.0	609 nm
BC13	105 ± 2 nm	1.395 ± 0.001	97.3	714 nm
substrate (boron silicate glass)	2 mm	1.530 ± 0.001	92.0	550 nm

transmission values were due to the tuned refractive indices, and the horizontal location of the maximum peak was due to altered film thickness, which would not affect transmission. Thus, by varying the concentration of base catalyst which results in modifications of porosity, it is possible to optimize the refractive index and percentage of transmission.

Conclusion

Porous silica thin films were prepared by sol–gel method by dip-coating technique in the presence of acid and base catalysts. The coatings showed variation in morphology depending on the nature of the catalyst used. While acid catalysis resulted in smoother surface, base-catalyzed coatings exhibited a coarse, porous surface. Infrared spectral analysis showed an increase in Si–O–Si peak intensity in the case of base catalysis, because an increase in condensation reaction of silanol group (Si–OH) results in coarse particles. As a result of coarse particle morphology, base-catalyzed samples exhibited larger surface area and pore volume, while acid-catalyzed samples showed lower surface area and pore volume because of smooth surface. Base-catalyzed silica coatings showed superior optical transmission, higher surface roughness, and lower refractive indices, while acid-catalyzed silica showed less porous and nonparticulate network structure with a lower optical transmission. Base-catalyzed samples provided a greater flexibility in controlling the particle size, pore size, refractive index, and hence optical coatings suitable for antireflective applications. However, the mechanical strength of the acid-catalyzed coatings was found to be superior than that of base-catalyzed coatings because of the stronger particle–particle binding. The present work shows that by controlling the porosity and particle size, it is possible to attain almost 99% transmission in the visible range. In general, this approach can be useful for preparing sol–gel based porous antireflective optical coatings.

References and Notes

- (1) Cao, M.; Song, X.; Zhai, J.; Wang, J.; Wang, Y. *J. Phys. Chem. B* **2006**, *110*, 13072.
- (2) Yoldas, B. E. *Appl. Opt.* **1980**, *19*, 1425.
- (3) Yoldas, B. E.; Partlow, D. P. *Appl. Opt.* **1984**, *Vol. 23*, 1418.

- (4) Thomas, I. M. *Appl. Opt.* **1988**, *27*, 3356.
- (5) Suzhu, Y.; Terence, K. S. W.; Kantisara, P.; Xiao, H. *J. Vac. Sci. Technol., B* **2002**, *20*, 2036.
- (6) Biswas, P. K.; Devi, P. S.; Chakraborty, P. K.; Chatterjee, A.; Ganguli, D.; Kamath, M. P.; Joshi, A. S. *J. Mater. Sci. Lett.* **2003**, *22*, 181.
- (7) Cook, L. M.; Lowdermilk, W. H.; Milam, D.; Swain, J. E. *Appl. Opt.* **1982**, *21*, 1482.
- (8) Floch, H. G.; Priotton, J.-J. *Ceram. Bullet.* **1990**, *69*, 1141.
- (9) Hiller, J. A.; Mendelsohn, J. D.; Rubner, M. F. *Nat. Mater.* **2002**, *1*, 59.
- (10) Liu, Y.; Ren, W.; Zhang, L.; Yao, X. *Thin Solid Films* **1999**, *353*, 124.
- (11) Thomas, I. M. *Appl. Opt.* **1992**, *31*, 6145.
- (12) Wu, G.; Wang, J.; Shen, J.; Zhang, Q.; Zhou, B.; Deng, Z.; Fan, B.; Zhou, D.; Zhang, F. *High Temp. - High Pressures* **2000**, *32*, 687.
- (13) Yang, H.-S.; Choi, S.-Y.; Hyun, S.-H.; Park, H.-H.; Hong, J.-K. *J. Non-Cryst. Solids* **1994**, *221*, 151.
- (14) Prevo, B. G.; Hwang, Y.; Velez, O. D. *Chem. Mater.* **2005**, *17*, 3642.
- (15) Janotta, M.; Katzir, A.; Mizaikoff, B. *Appl. Spectrosc.* **2003**, *57*, 823.
- (16) Wu, G.; Wang, J.; Shen, J.; Yang, T.; Zhang, Q.; Zhou, B.; Deng, Z.; Fan, B.; Zhou, D.; Zhang, F. *Mater. Sci. Eng., B* **2000**, *78*, 135.
- (17) Bautista, M. C.; Morales, A. *Sol. Energy Mater. Sol. Cells* **2003**, *80*, 217.
- (18) Takada, S.; Hataa, N.; Seino, Y.; Fujii, N.; Kikkawa, T. *J. Appl. Phys.* **2005**, *97*, 113504.
- (19) Thomas, I. M. *Appl. Opt.* **1986**, *25*, 1481.
- (20) Du, X. M.; Almeida, R. M. *J. Sol-Gel Sci. Technol.* **1997**, *8*, 377.
- (21) Graubner, V. M.; Jordan, R.; Nuyken, O.; Schnyder, B.; Lippert, T.; Kotz, R.; Wokaun, A. *Macromolecules* **2004**, *37*, 5936.
- (22) Brinker, C. J.; Scherer, G. W. *Sol-Gel Science: The Physics and Chemistry of Sol-Gel Processing*; Academic Press, Inc.: New York, 1990.
- (23) Iler, R. K. *The Chemistry of Silica*; Wiley: New York, 1979.
- (24) Bhagat, S. D.; Kim, Y.-H.; Ahn, Y.-S.; Yeo, J.-G. *Microporous Mesoporous Mater.* **2006**, *96*, 237.
- (25) Wang, J.; Wu, G.; Shen, J.; Yang, T.; Zhang, Q.; Zhou, B.; Deng, Z.; Fan, B.; Zhou, D.; Zhang, F. *J. Sol-Gel Sci. Technol.* **2000**, *18*, 219.
- (26) Ulmeanu, M.; Serghei, A.; Mihalescu, I. N.; Budau, P.; Enachescu, M. *Appl. Surf. Sci.* **2000**, *165*, 109.
- (27) Beckmann, P.; Spizzichino, A. *The Scattering of Electromagnetic Wave from Rough Surface*; Pergamon: Oxford, U.K., 1963.
- (28) Krc, J.; Smole, F.; Topic, M. *Prog. Photovoltaics* **2003**, *11*, 15.
- (29) Poruba, A.; Fejfar, A.; Remes, Z.; Springer, J.; Vanecek, M.; Kocka, J.; Meier, J.; Torres, P.; Shah, A. *J. Appl. Phys.* **2000**, *88*, 148.
- (30) Xu, Y.; Fan, W. H.; Li, Z. H.; Wu, D.; Sun, Y. H. *Appl. Opt.* **2003**, *42*, 108.
- (31) Manificier, J. C.; Gasiot, J.; Fillard, J. P. *J. Phys. E* **1976**, *9*, 1002.
- (32) Swanepoel, R. *J. Phys. E* **1983**, *16*, 1214.
- (33) Kim, G.-S.; Hyun, S.-H. *J. Non-Cryst. Solids* **2003**, *320*, 125.
- (34) Cheng, N.-S.; Law, A. W.-K. *Powder Technol.* **2003**, *129*, 156.